JTTEE5 15:657-662
DOI: 10.1361/105996306X147171
1059-9630/$19.00 © ASM International

Thermomechanical Behavior of Nanostructured Plasma Sprayed Zirconia Coatings

R. Soltani, E. Garcia, T.W. Coyle, J. Mostaghimi, R.S. Lima, B.R. Marple, and C. Moreau

(Submitted February 21, 2006; in revised form April 17, 2006)

Retaining nonmelted nanoparticles of zirconia in nanostructured coatings has been a challenge in the past. Recently an air plasma spray process was developed to produce coatings that retain up to 30–35% by volume nonmelted particles, resulting in a unique structure. The creep/sintering behavior of such thermal barrier coatings deposited from nanostructured feedstock has been measured and compared with deposits produced from hot oven spherical particles (HOSP). Both feedstocks contain 6–8 wt.% Y_2O_3 as a stabilizer. Flexure and compression creep testing were conducted under several different loads and temperatures to obtain creep exponents and parameters.

Keywords ceramic oxide layers, coatings for engine components, coatings for gas turbine components, spray forming of combustion chambers

1. Introduction

Plasma sprayed thermal barrier coatings for different applications are still being developed; however, there is not much information on high temperature properties of these new coatings. Operating temperatures for zirconia coatings are usually around 1000 °C, considering applications such as diesel engines combustion chambers. The presence of relatively high compressive stresses at the coating surface leads to stress relaxation by creep and/or sintering. Shrinkage at high temperatures may lead to crack initiation and propagation during cooling, causing spallation of the coating and consequently shortening the lifetime of the deposit.

The creep/sintering behavior of monolithic and plasma sprayed zirconia has been investigated by several researchers (Ref 1-10). Elastic modulus, hardness, and thermal conductivity vary with temperature, and so affect the residual stresses present at the operating temperature (Ref 1, 11). Sintering at service temperatures may heal microcracks and eliminate some porosity, creating a denser structure, which could be an advantage in reducing oxygen gas (not the ion) penetration to the bond coat and reducing its oxidation. Unfortunately, upon cooling microcracks reappear due to high thermal gradients. Eventually the coating becomes sufficiently damaged as spalling occurs. The thickness of the coating is another important factor; in some applications depositions of more than 1 mm in thickness are required to increase protection and reduce heat transfer. The thicker the coating, the greater the thermal gradients present during service, which results in higher stresses within the coating (Ref 3).

Therefore, investigating high temperature properties of thermal barrier coatings is a priority in the development of new top coat structures. Bimodal structured thermal barrier coatings can provide the improved performance of an alternative material without the necessity of redesigning the entire component. There are several methods to produce nanostructured coatings, including thermal spray processes. Researchers have shown that nanostructured coatings can exhibit better properties than conventional coatings of the same composition (Ref 12-18).

In the current work, partially stabilized zirconia (PSZ) coatings were deposited by air plasma spraying. Two different types of powder feed stock were used, a conventional micron particle size powder and a nanostructured particle powder. The influence of the powder type on the thermomechanical behavior of the coatings was investigated.

2. Experimental Procedures

Two commercially available 6-8 wt.% Y_2O_3-PSZ powders were used to deposit coatings by air plasma spraying. A nanostructured powder (Nanox S4007, Inframat Corp., CT) was deposited using the F4-MB (Sulzer-Metco, NY) torch. This powder consists of porous agglomerated particles 15-150 μm in diameter made up of crystallites on the order of 200 nm, as shown in the right side of Fig. 1. A powder consisting of hollow spherical particles (204B-NS, Sulzer-Metco, NY) was deposited with an SG-100 (Praxair, Concord, NH) plasma torch. The particle size of this HOSP powder was 45-75 μm as shown in the left side of Fig. 1.

The substrates were carbon steel plates with dimensions of 50 × 50 × 4 mm (W × L × H). Before coating, the surface of the

This article was originally published in *Building on 100 Years of Success, Proceedings of the 2006 International Thermal Spray Conference* (Seattle, WA), May 15-18, 2006, B.R. Marple, M.M. Hyland, Y.-Ch. Lau, R.S. Lima, and J. Voyer, Ed., ASM International, Materials Park, OH, 2006.

R. Soltani, E. Garcia, T.W. Coyle, and **J. Mostaghimi,** Centre for Advanced Coating Technologies, University of Toronto, Ontario, Canada; **R.S. Lima, B.R. Marple,** and **C. Moreau,** National Research Council Canada, Boucherville, Québec, Canada. Contact e-mail: rsoltani@mie.utoronto.ca.

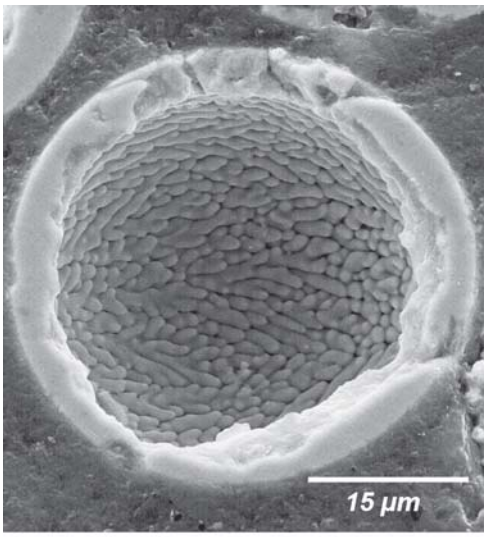

(a)

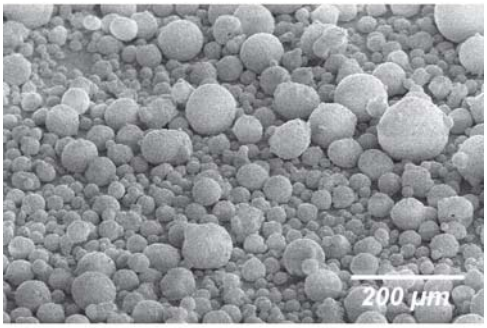

(b)

Fig. 1 (a) Typical SEM image of 204B-NS feedstock particle, and (b) Nonox S4007

substrates was alumina grit blasted to an rms roughness of approximately 4 μm as measured using a Surfometer (Precision Devices Inc., MI). The thickness of the coating was more than 3 mm. Samples then were cut to nominally 3 × 4 × 40 mm (H × W × L). The substrates were detached by reducing the thickness of the carbon plates with a precision saw to 1 mm. Because no bond coat was applied, and residual stresses were high due to the large thickness, the coatings could then be separated from the substrate.

The powder and coating microstructures were examined by field emission scanning electron microscopy (FE-SEM, Hitachi S-4500, Tokyo, Japan) operating under low accelerating voltage conditions. An image analyzer (Clemex Vision Professional software, QC, Canada) was used to measure the average porosity of each sample and the nonmelted nanoparticle area fraction for the nanostructured deposit. The pore size and distribution were measured with a mercury intrusion porosimeter (MIP, Auto Pore III, Micromeritics Instrument Corp., GA). The chemical composition of the powders was obtained from flame photometry (FP) and inductively coupled plasma for atomic emission spectroscopy (ICP (-AES, IRIS Advantage, Thermo Jarrell Ash Corp., MA). Creep tests were conducted employing 4-point bend and compression tests. Details have been presented elsewhere (Ref 19).

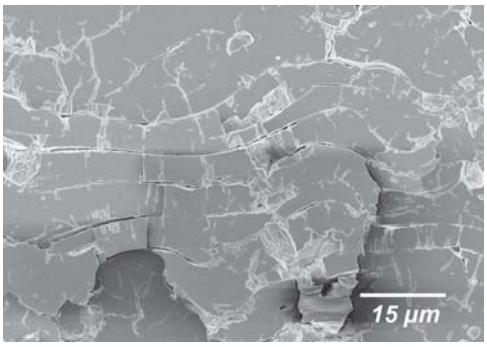

Fig. 2 SEM image of a polished surface of 204B-NS deposit showing layers of splat

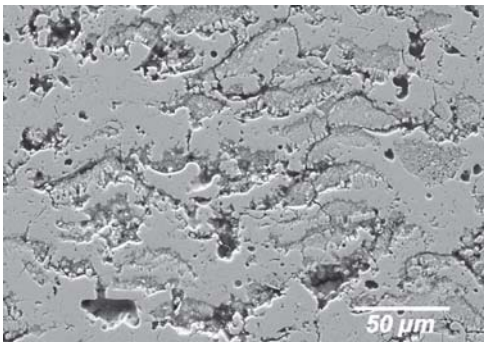

Fig. 3 SEM image of a polished surface of nanostructured deposit revealing melted and unmelted areas

3. Results and Discussion

3.1 Characterization

Prior to conducting creep tests, scanning electron microscopy (SEM) images of the conventional and nanostructured coatings deposited using 204B-NS and Nanox powders were taken as shown in Fig. 2 and 3, respectively. The nanostructured sample had a unique arrangement of nonmolten nanoparticles occupying a significant volume fraction of the sample. Figure 3 shows there is a significant presence of nonmolten nano-YSZ feedstock particles embedded in the coating microstructure. The thin shell geometry of the 204B-NS particles increases the probability of having fully melted particles when using this feedstock, which results in a high flattening ratio and very thin (1-1.5 μm) final splats in the coating. A well-layered deposit with a very low amount of globular pores is the final structure of the coating (Fig. 2). Zirconia is an effective thermal barrier due to its low conductivity; therefore slow heat transfer to the core of a solid particle may result in partially melted particles.

Porosity and nonmolten nanoparticle areas in deposits were investigated by image analysis (Table 1). From each sample 20 images were taken. Results showed that the porosity of the nanostructured sample was more than twice that in the 204B-NS coating and nonmolten nanoparticles occupied an area of 30-35%. To measure these areas all of them were recolored manually then the overall area was calculated with image analyzer software;

Table 1 Porosity and nano area percentage of nanostructured and 204B-NS coatings

Coating	Porosity, %	Nano, %	Density, g/cm^3
204B-NS	11 ± 1	0	5.07
Nanox	>25 ± 2	30–35	4.11

therefore underestimation of nonmolten nanoparticle area measurement should be considered due to low magnification of SEM images. The nanopores within the nonmelted nanoparticle areas could not be resolved in the low magnification images used for the image analysis. Therefore, it is likely that the porosity results underestimate the level of porosity actually present in the coating.

To obtain information on the pore size and distribution, mercury intrusion porosimetry tests were conducted. The results showed there was a wider range of pore sizes in the nanostructured coating and that this coating had more porosity (a larger amount of mercury intrusion), as shown in Fig. 4.

A comparison of Fig. 2 and 3 reveals that the porosity type in 204B-NS sample mostly consists of very thin gaps between splats, whereas in Nanox coating there are big planar and globular pores between nonmolten nanoparticle areas and conventional splats. The narrow pore size distribution of 204B-NS deposit in Fig. 4 could be an indication of this structure.

Compositional analysis was performed to investigate the levels of several common impurities in the two feedstocks. No major differences between the two materials were found (Table 2). Particular components such as silica, alumina, and titania, which may create a glassy phase at grain boundaries, were present in almost the same amounts in both powders. Therefore, if these constituents have any effect on the creep/sintering behavior of the samples, it is expected that it would be similar for both. Therefore a comparison based on structural considerations should be valid.

3.2 Creep

Creep tests on 204B-NS freestanding deposits were conducted employing a SiC four-point flexure fixture under a range of stresses and temperatures to obtain creep exponents and activation energy values for the coatings as shown respectively in Figs. 5 and 6. These samples were strong enough to withstand loads up to almost 50 N in this test method. Samples show a high strain rate in the primary phase. With increasing strain, the creep rate is reduced dramatically, approaching a steady state rate. Raising the stress level at constant temperature (1000 °C) results in an increased creep strain, but the creep rate in the secondary phase does not change significantly. This indicates a low dependency on stress (Fig. 5).

Figure 6 shows the creep strain of the same material at a range of temperatures. A higher dependency on temperature than stress is observed.

Because the strength of nanostructured samples was not enough to perform flexure test on them with this set up, a compression technique was used to measure the creep behavior of these deposits. Based on previous experiments, these two methods showed an acceptable consistency in results. Nutt and Lipetzky found the same reliability for alumina reinforced with SiC whiskers (Ref 20).

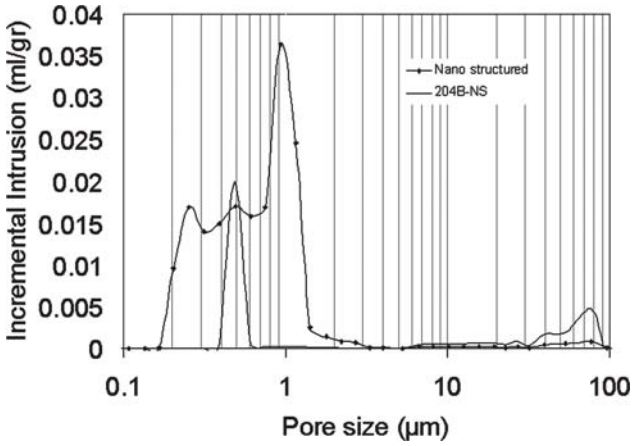

Fig. 4 Mercury porosimetry of nanostructured and 204B-NS coatings showing higher porosity and a wider pore size range for the nanostructured deposit

Table 2 Chemical composition of the two feedstock powders; nanostructured and 204B-NS

	Nanox, %	204B-NS, %	Technique
Al_2O_3	0.66	0.66	ICP-AES
CuO	0.007	0.008	ICP-AES
CaO	0.025	0.026	ICP-AES
Fe_2O_3	0.006	0.009	ICP-AES
HfO_2	1.74	1.52	ICP-AES
P_2O_5	0.04	0.04	ICP-AES
SiO_2	0.12	0.11	ICP-AES
TiO_2	0.06	0.14	ICP-AES
Y_2O_3	6.43	7.30	ICP-AES
Na_2O	0.03	0.02	FP

ICP, Inductively coupled plasma for atomic emission spectroscopy; FP, Flame photometry

Figures 7 and 8 show the creep strain of nanostructured coatings under a range of stresses and temperatures for two days. As is clear, this nanostructured coating, in spite of applying much lower stresses, exhibits about an order of magnitude higher creep strain than the 204B-NS deposits.

As was observed for the 204B-NS samples, the nanostructured deposits exhibit primary and secondary creep. As load and temperature of the test conditions are increased, the amount of creep strain rises. Again, temperature has a more significant effect, as is clear from Fig. 8.

From the creep data, using the power-law creep ($\hat{O} = A\ \sigma^n$) and Arrhenius ($\dot{\varepsilon} = A\exp -Q/RT$) equations, stress exponents and activation energies for the coatings were calculated where $\hat{O}$ is creep strain, A is a constant, s applied stress in MPa, $\dot{\varepsilon}$ strain rate, Q activation energy, R gas constant, and T temperature in Kelvin (Fig. 9 and 10). The nanostructured deposit shows a slightly lower activation energy of 165 ± 40 KJ/mol compared with 192 ± 25 KJ/mol for the 204B-NS sample; however considering the interval of values they may not be very different. In addition, the stress exponent for the nanostructured specimens (n~2) is larger than for the 204B-NS (n~1). This difference in creep exponents may be an indication of different creep mechanisms active in the two types of samples. To investigate the dominant mechanisms

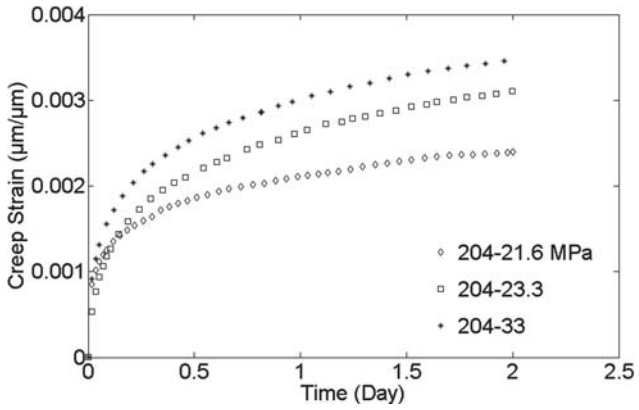

Fig. 5 Creep strain of 204B-NS sample under different stress levels at 1000 °C for two days

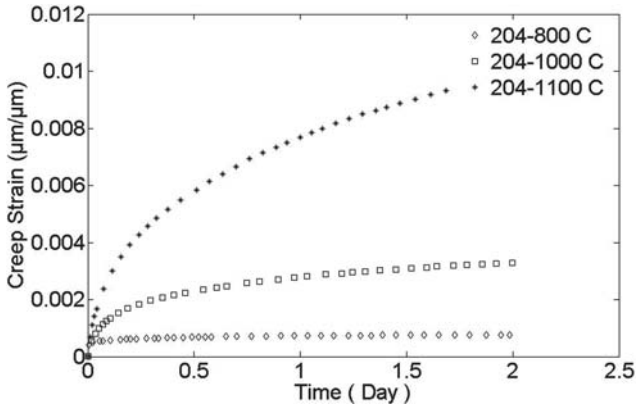

Fig. 6 Creep strain of 204B-NS samples under 24 MPa for two days at different temperatures

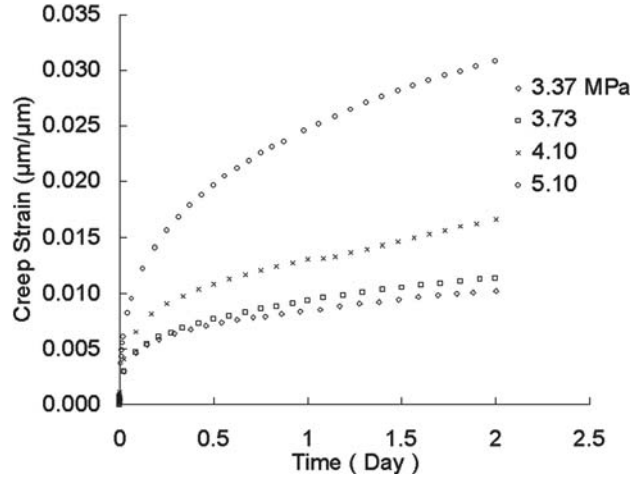

Fig. 7 Compression creep strain of nanostructured samples under different stresses at 1000 °C

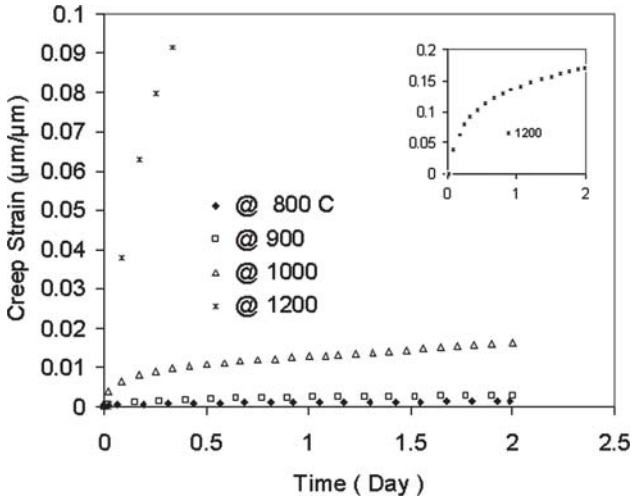

Fig. 8 Creep strain of nanostructured samples at different temperatures under ~4 MPa compressive stress

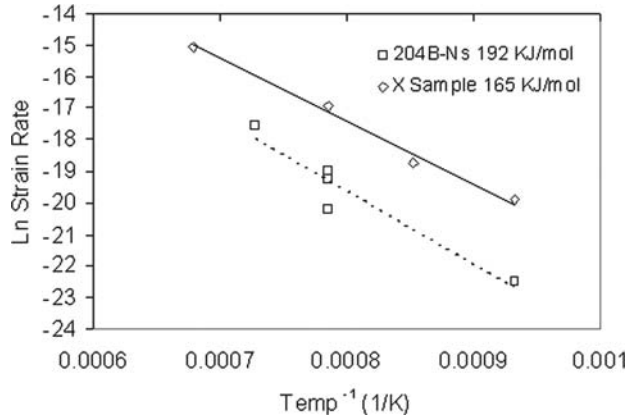

Fig. 9 Calculation of activation energy of nanostructured and 204B-NS samples, 165 ± 40 and 192 ± 25 KJ/mol, respectively

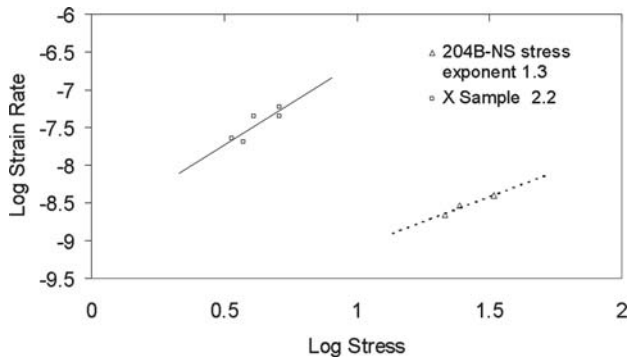

Fig. 10 Determination of stress exponents for 204B-NS and nanostructured samples; n = 1.3 and 2.2, respectively.

in each sample SEM work was done and some of these images are shown in Fig. 11-13.

On the fracture surface of a 204B-NS sample fractured after creep, three different microstructural changes described by T.W. Clyne are observed (Ref 12): intrasplat and intersplat grain growth and microcrack healing. Surface diffusion leads to grain boundary grooving, touching and necking of columnar grains across microcracks, and consequently the closure of some mi-

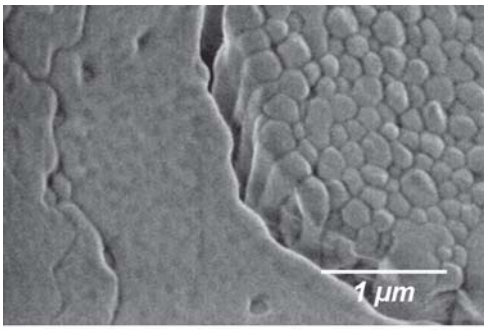

(a)

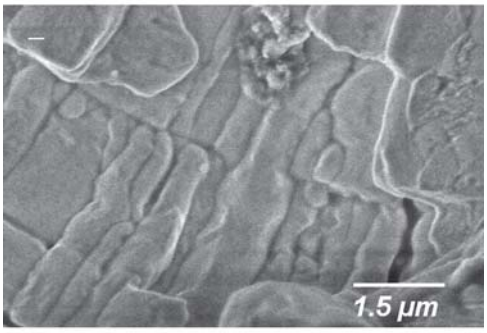

(b)

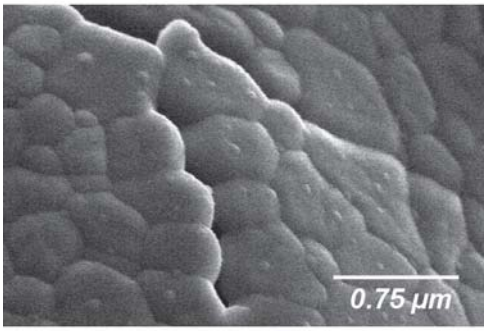

(c)

Fig. 11 After creep SEM images of 204B-NS (2 days at 1000 °C under 21 MPa); (a) intrasplat grain growth, (b) intersplat grain growth, and (c) microcrack healing

crocracks. The SEM images in Fig. 11 show intra (a) and inter (c) splat grain growth, and microcrack healing (b).

The nanostructured sample has a unique array of splats and nonmolten nanoparticles as shown in Fig. 12. The structure appears to consist of one or two successive layers of conventional splats and then a deposit of nanoparticles. SEM investigation showed that microcrack healing still occurred in this structure; however, due to the very low density of microcracks in the structure, the affect of this would be much less significant than in the 204B-NS coatings. Columnar grain growth was also observed; however, because most splats were separated from one another by regions of nonmolten nanoparticles, intersplat grain growth was limited. Figure 13 shows the nonmolten nano particles (in a higher magnification) indicating that even after 2 days at 1000 °C and under compressive stresses these particles are still present in the coating and sintering processes have not vanished

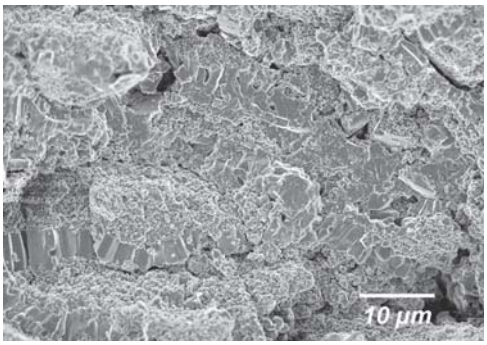

Fig. 12 SEM image of fracture surface of nanostructured coating broken after creep (2 days at 1000 °C under 5.1 MPa)

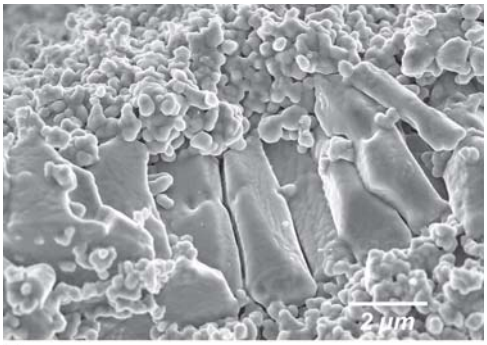

(a)

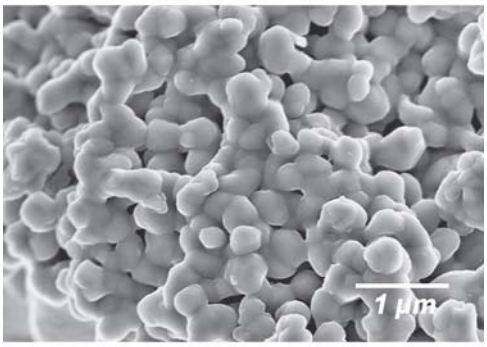

(b)

Fig. 13 SEM images of nanostructured deposit after creep testing

them completely. The porosity of the nanostructured sample is clearly higher than the 204B-NS sample.

Based on SEM examinations, grain boundary sliding and rearrangement of the nanoparticles seem to be the dominant mechanisms responsible for the high creep strain of the nanostructured coating (Ref 21-23).

As seen in Fig. 13, extensive regions of nanoparticles were still present after creep testing, and a large amount of nanoporosity remained among these particles.

4. Conclusions

Nanostructured zirconia thermal barrier coatings were successfully deposited with more than 30% preserved nonmolten

nanoparticles in the coating. The creep behavior of this structure was characterized and compared with a conventional coating. Results showed a higher creep strain for the nanostructured sample than for the conventional with activation energies of 165 and 192 KJ/mol and a stress exponent of 2.2 and 1.3 for the nanostructured and conventional deposits, respectively. The higher creep rate of the nanostructured sample would result in more rapid stress relaxation at elevated temperatures in service. This may result in the development of tensile stresses at the surface of the coating upon cooling, which could in turn lead to cracking and spallation of the coating. However, nanostructured ceramic coatings typically exhibit higher toughness and higher bond strengths than conventional coatings (Ref 24, 25). In addition, the porous nonmolten nanoparticle regions within the coating microstructure would exhibit a very low elastic modulus, increasing the compliance of the coating. Therefore, although these nano-YSZ coatings may be more likely to develop tensile surface stresses under service conditions, they may withstand these stresses better than conventional TBCs. Thermal cycle tests are pending to examine the performance of the nanostructured coatings under such conditions.

References

1. D. Zhu and R.A. Miller, Determination of Creep Behavior of Thermal Barrier Coatings Under Laser Imposed Temperature and Stress Gradients, *NASA Technical Memorandum 113169,* ARL-TR-1556, 1997
2. D. Zhu and R.A. Miller, Sintering and Creep Behavior of Plasma-Sprayed Zirconia and Hafnia-Based Thermal Barrier Coatings, *Surf. Coat. Technol.,* 1998, **108–109,** p 114-120
3. E.F. Rejda, D.F. Socie, and T. Itoh, Deformation Behavior of Plasma-Sprayed Thick Thermal Barrier Coatings, *Surf. Coat. Technol.,* 1999, **113,** p 218-226
4. A.H. Chokshi, Diffusion Creep in Oxide Ceramics, *J. Eur. Ceram. Soc.,* 2002, **22,** p 2469-2478
5. A.H. Chokshi, Diffusion, Diffusion Creep and Grain Growth Characteristics of Nanocrystalline and Fine-Grained Monoclinic, Tetragonal and Cubic Zirconia, *J. Scripta Mater.,* 2003, **48,** p 791-796
6. R. Schaller and M. Daraktciev, Mechanical Spectroscopy of Creep Appearance in Fine-Grained Yttria-Stabilized Zirconia, *J. Eur. Ceram. Soc.,* 2002, **22,** p 2461-2467
7. M.J. Andrews, M.K. Ferber, and E. Lara-Curzio, Mechanical Properties of Zirconia-Based Ceramics as Functions of Temperature, *J. Eur. Ceram. Soc.,* 2002, **22,** p 2633-2639
8. K. Kokini, Y.R. Takeuchi, and B.D. Choules, Surface Thermal Cracking of Thermal Barrier Coatings Owing to Stress Relaxation: Zirconia vs. Mullite, *Surf. Coat. Technol.,* 1996, **82,** p 77-82
9. L. Vasylkiv, Y. Skka, and V.V. Skorokhod, Low-temperature Processing and Mechanical Properties of Zirconia and Zirconia-Alumina Nanoceramics, *J. Am. Ceram. Soc.,* 2003, **86**(2), p 299-304
10. M. Daraktchiev and R. Schaller, High-temperature Mechanical Loss Behavior of 3 mol% Yttria-Stabilized Tetragonal Zirconia Polycrystals, 3Y-TZP, *J. Phys. Stat. Sol.,* 2003, **2,** p 293-304
11. R.S. Lima, A. Kucuk, and C.C. Berndt, Bimodal Distribution of Mechanical Properties in Plasma Sprayed Nanostructured Partially Stabilized Zirconia, *J. Mater. Sci. Eng. A,* 2002, **327,** p 224-232
12. J.A. Thompson and T.W. Clyne, The Effect of Top Coat Sintering on Ceramic Spallation in Plasma Sprayed Thermal Barrier Coatings, The 13th International Conference on Surface Modification Technology (SMT XIII), Convention City, Singapore, 1999, p 177-182
13. L. Shaw, D. Goerman, R. Ren, and M. Gell, The Dependency of Microstructure and Properties of Nanostructured Coatings on Plasma Spray Conditions, *Surf. Coat. Technol.,* 2000, **130,** p 1-8
14. M. Gell, E.H. Jordan, Y.H. Sohn, and D. Goerman, Development and Implementation of Plasma Sprayed Nanostructured Ceramic Coatings, *Surf. Coat. Technol.,* 2001, **146-147,** p 48-54
15. H. Chen and C.X. Ding, Nanostructured Zirconia Coating Prepared by Atmospheric Plasma Spraying, *Surf. Coat. Technol.,* 2002, **150,** p 31-36
16. H. Chen and C.X. Ding, Micro-structural Characterization of Plasma Sprayed Nanostructured Zirconia Powders and Coatings, *J. Eur. Ceram. Soc,* 2003, **23,** p 491-497
17. M. Gell and L. Shaw, Fabrication and Evaluation of Plasma Sprayed Nanostructured Alumina-Titania Coatings with Superior Properties, *J. Mater. Sci. Eng. A,* 2001, **301,** p 80-89
18. R.S. Lima and C.C. Berndt, Evaluation of Microhardness and Elastic Modulus of Thermally Sprayed Nanostructured Zirconia Coatings, *Surf. Coat. Technol.,* 2001, **135,** p 166-172
19. R. Soltani, T.W. Coyle, J. Mostaghimi, Thermomechanical Behaviour of Bimodal Structured Thermal Barrier Coatings, International Thermal Spray Conference, May 10–12, 2004 (Osaka, Japan)
20. S.R. Nutt and P.L. Lipetzky, Creep Deformation of Alumina-SiC Composites, *J. Mater. Sci. Eng. A,* 1990, **126,** p 165-172
21. H. Echsler, D. Renusch, and M. Schutze, Mechanical Behaviour of as Sprayed and Sintered Air Plasma Sprayed Partially Stabilized Zirconia, *J. Mater. Sci. Technol.,* 2004, **20,** p 869-876
22. M. Ahrens, S. Lampenscherf, R. Vaben, and D. Stover, Sintering and Creep Processes in Plasma-Sprayed Thermal Barrier Coating, *J. Therm. Spray Technol.,* 2004, **13**(3), p 432-442
23. G. Thurn, G.A. Schneider, and F. Aldinger, High-Temperature Deformation of Plasma Sprayed ZrO_2 Thermal Barrier Coating, *J. Mater. Sci. Eng. A,* 1997, **233,** p 176-182
24. P. Bansal, N. Padture, and A. Vasiliev, Improved Interfacial Mechanical Properties of Al_2O_3-13TiO_2 Plasma-Sprayed Coatings Derived from Nanocrystalline Powders, *Acta Mater.,* 2003, **51,** p 2959-2970
25. H. Luo, D. Goberman, L. Shaw, and M. Gell, Indentation Fracture Behavior of Plasma-Sprayed Nanostructured Al_2O_3-13wt%TiO_2 Coatings, *J. Mater. Sci. Eng. A,* 2003, **346,** p 237-245